Weyl nodal point-line Fermion in ferromagnetic Eu_5Bi_3

Hongbo Wu[1], Da-Shuai Ma[1], Botao Fu[2],* Wei Guo[1], and Yugui Yao[1]*

[1] *Key Laboratory of advanced optoelectronic quantum architecture and measurement (MOE), Beijing Key Laboratory of Nanophotonics and Ultrafine Optoelectronic Systems, School of Physics, Beijing Institute of Technology, Beijing 100081, China*

[2] *College of Physics and Electronic Engineering, Center for Computational Sciences, Sichuan Normal University, Chengdu, 610068, China*

E-mail: fubotao2008@gmail.com; ygyao@bit.edu.cn

Abstract

Based on *ab initio* calculations and low-energy effective $\boldsymbol{k}\cdot\boldsymbol{p}$ model, we propose a type of Weyl nodal point-line fermion, composed of 0D Weyl points and 1D Weyl nodal line, in ferromagnetic material Eu_5Bi_3. In the absence of spin-orbital coupling (SOC), the spin-up bands host a pair of triply degenerate points together with a unique bird-cage like node structure. In the presence of SOC with (001) magnetization, each triplet point splits into a double Weyl point and a single Weyl point accompanied by two nodal rings, forming two sets of Weyl nodal point-line fermions near the Fermi level. The novel properties of Weyl nodal point-line fermion are explored by revealing the unusual Berry curvature field and demonstrating the pinned chiral surface states with exotic Fermi arcs at different planes. Moreover, a large anomalous Hall conductivity of -260 $(\hbar/e)(\Omega\mathrm{cm})^{-1}$ parallel to [001] direction is predicted. Our work offers a new perspective for exploring novel topological semimetal states with diverse band-crossing dimensions, and provides an ideal material candidate for future experimental realiztion.

Topological semimetals (TSMs), emerging as new types of topological states, have recently attracted plenty of interest due to their physical meanings as counterparts for fundamental particles in field theory such as Weyl fermion and Dirac fermion[1–10] and also due to their fascinating properties like chiral anomaly,[11–14] surface magnetism/superconductivity[15–18] and 3D quantum hall effect (QHE),[19–21] etc. The band structures of TSM materials possess nontrivial band crossings close to the Fermi level and can be characterized by various topological invariants. Depending on the dimensionality of the band crossings, TSM states can be classified into zero-dimensional (0D) nodal point,[22–24] one-dimensional (1D) nodal line[25–30] and two-dimensional (2D) nodal surface[31–33] semimetals. The band crossings with distinctive dimensions lead to various topology and interesting physical properties.

Under broken time reversal (T) or space inversion (P) symmetry, Weyl semimetals (WSMs) that host twofold band-crossing points at the Fermi level can be achieved in magnetic or noncentrosymmetric materials.[34–38] Weyl point (WP) and Weyl nodal line (WNL) semimetals are currently the most prominent compositions of WSMs.[23,24,27] The topological nature of 0D WPs can be characterized by the non-zero chern number and exotic surface Fermi arcs.[39–42] When an additional rotation symmetry exists (e.g. C_3, C_4, C_6), multiple WPs will merge together at the rotation-invariant axis to create a high chern number Weyl fermion, which exhibits parabolic or cubic dispersion.[43–53] Unlike the WP semimetal, a WNL semimetal possesses a closed loop of double degenerate points in the momentum space and can be diagnosed by a quantized Berry phase through SdH oscillation experiment[28] or a flat "drumhead"-like surface state by ARPES.[54–56] A WNL structure is generally protected by a mirror or slide mirror symmetry[57,58] under strong SOC effect. The individual WP semimetal and WNL semimetal have been widely studied and part of them have already been observed in recent experiments.[4,23,24,38,42,55,59,60] Motivated by present fascinating topological harvest, we ask a question that can those topological semimetal states with diverse dimensions coexist in one system and what novel properties it will bring about if it exists.

In this paper, based on first-principles calculations and effective $\boldsymbol{k}\cdot\boldsymbol{p}$ model, we propose a

concept of Weyl nodal point-line (WNPL) fermion in a ferromagnetic material Eu_5Bi_3, which consists of a pair of 0D WPs and a 1D WNL that couple together in one physics system and can be created and annihilated simultaneously via band inversion mechanism. In the case without SOC , the spin-polarized bands of Eu_5Bi_3 host a pair of triple points in HKH′ path protected by rotation symmetry. Contrast to other known triplet points in nonmagnetic and non-centrosymmetric materials,[47–52] this two magnetic triplet points connect to each other by an unique bird-cage like node structure centering at K point. When SOC effect is included and consider (001) magnetization, a topological phase transition happens. Each triplet point splits into a double Weyl point and a single Weyl point accompanied by two homocentric WNLs at $k_z = 0$ plane, thus forming two sets of composite WNPL fermions around the Fermi level. Moreover, we build a low-energy effective $\boldsymbol{k}\cdot\boldsymbol{p}$ model that can capture the novel topological nature of the WNPL fermion. In particular, we discover that the WNPL fermion possesses strong coupling behavior that gives rise to pinned chiral surface states with exotic Fermi arcs at different projection planes.

The rare-earth bismuthide Eu_5Bi_3 crystallizes in a stacked hexagonal lattice with the space group $P6_3/mcm$ (No. 193). It hosts a point group D_{6h} that includes a six-fold rotation axis C_{6z}, a horizontal mirror σ_h and six vertical mirror σ_v. The geometric structures of Eu_5Bi_3 are shown in Figs. 1 (a)-(b), where Eu atoms take two types of Wyckoff positions $4c$ (1/3, 2/3, 0) and $6g$ (0.251, 0, 1/4), and Bi atoms take one type of Wyckoff position $6g$ (0.609, 0, 1/4). Meanwhile, the hexagonal bulk Brillouin zone with high-symmetry $\boldsymbol{k}$ paths and projected (001)/(100) surface Brillouin zone are illustrated in Fig. 1(c). The optimized lattice constants of Eu_5Bi_3 are $a = 9.68$ Å and $c = 7.36$ Å, in good agreement with the experimental data.[61] The macroscopical ferromagnetic states of Eu_5Bi_3 had been observed below 101 K.[61] Our first-principles calculations[62] also confirm that the ferromagnetic (FM) state is the ground state with lowest total energy and each Eu atom possesses a magnetic moment of $\sim 7.0\ \mu_B$, which is in good accordance with the experimental value.[61] In addition, the calculated magnetic crystalline anisotropy energy is less than 0.05 meV/atom between

out-plane and in-plane magnetization, indicating the switch of magnetization direction by an external magnetic field is operable.

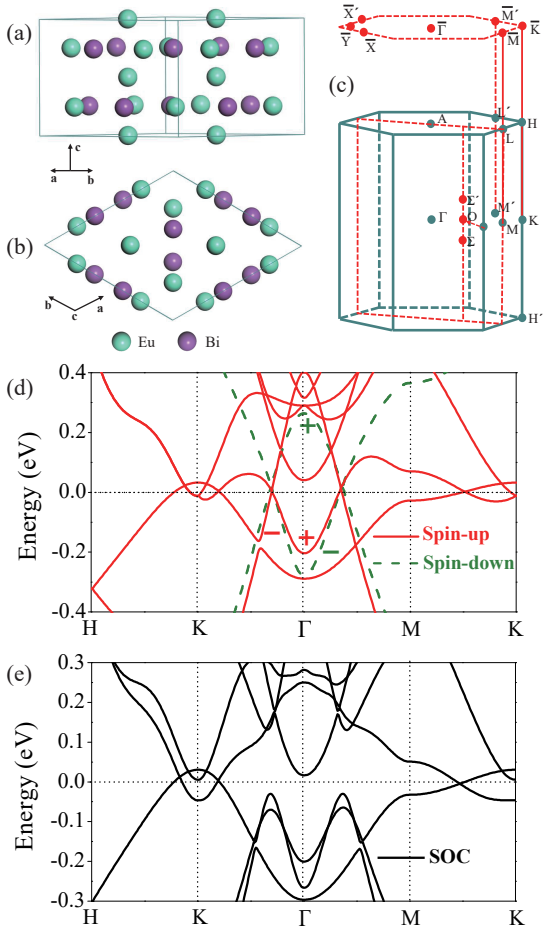

Figure 1: Crystal structure, Brillouin zone and band structure of Eu_5Bi_3. (a) Side view and (b) top view of the crystal structure of Eu_5Bi_3 with space group $P6_3/mcm$ (No. 193). (c) The hexagonal Brillouin zone, the high-symmetry $\boldsymbol{k}$ path and the projected surface Brillouin zone of (001) and (100) planes. The red dashed lines denote the projected surface Brillouin. (d) Spin-polarized band structure of Eu_5Bi_3. (e) SOC band structure of Eu_5Bi_3 with (001) magnetization. The Fermi level is shifted to zero in (d) and (e).

The spin-polarized band structure of Eu_5Bi_3 without SOC is demonstrated in Fig. 1 (d). In the absence of SOC, spin is a good quantum number. We notice that both spin-up and spin-down channels exhibit topological metal states with various band crossings near the Fermi level. For the spin-down bands (green dashed line) at low-energy part, the conduction band crosses with the valence band forming a clean and large-size nodal line structure encircling Γ point. It is easy to confirm that this nodal line structure, located at

$k_z = 0$ plane, is protected by the horizontal mirror σ_h because of its opposite eigenvalues. Similarly, for the spin-up bands (red solid line), a nodal line structure lying on $k_z = 0$ plane emerges due to the band inversion around Γ point.

As both the Eu and Bi atoms belong to heavy elements that have non-negligible SOC effect, we then switch on the SOC and consider (001) magnetization. The band structure with SOC is displayed in Fig. 1 (e). The point group of Eu_5Bi_3 transforms from D_{6h} into C_{6h}, where the vertical mirror σ_v is broken but the horizonal mirror σ_h is left. Due to the SOC effect, the spin s_z is no longer a good quantum number. Thus, the spin-up and spin-down bands with same eigenvalue of σ_h that cross each other at the Fermi level in Fig. 1 (d) will inevitably couple each other, and a gap is opened around Γ point as shown in Fig. 1 (e).

In this section, we focus on the band structures of Eu_5Bi_3 around K point. In the absence of SOC, the little group along H-K-H′ path is C_{3v}, which hosts a two-dimensional and a one-dimensional irreducible representations that can support a two-fold and a singlet band degeneracy, respectively. Consequently, as shown in Fig. 2 (a), a doubly degenerate conduction band (Γ_3) inverts with a singlet valence band (Γ_2) and forms a pair of triplet degenerate points (TDPs) along H-K-H′ path. The negative band gap at K point from the band inversion is sensitive to Hubbard U due to strongly correlated f electrons in Eu atoms, nevertheless, we have confirmed the band inversion does happen within a wide and reasonable on site Coulomb interaction (see the Supporting Information Fig.S 1).[62] With inset in Fig. 2 (a), we demonstrate the dispersion of the TDP in K_{xy} direction, and find a linear band crossing superimposed with a quadratic band which is similar to that in non-magnetic TDP systems.[50]

As shown in Figs. 1 (c), the M-K-M′ path locates at the intersection of σ_h invariant plane (ΓMKM′) and σ_v invariant plane (MKHL). Thus, the energy bands along M-K-M′ can be represented by the eigenvalues of σ_h and σ_v, respectively as shown in Fig. 2 (b). We discover two conduction bands (Λ_2, Λ_3) possess positive eigenvalue of σ_h, while the valence

band (Λ_1) has negative eigenvalue. As a result, at the σ_h invariant plane ΓMKM′ , the crossing points of bands Λ_2 and Λ_1 have to form a nodal line structure (NL1 in Fig. 2 (e)) centered at K point. Similarly, the crossing points between bands Λ_3 and Λ_1 also form a nodal line structure (NL2). The NL1 structure encompasses NL2 at k_z=0 plane, and NL1 is more closer to Fermi level than NL2. The eigenvalues of σ_v are also calculated as shown in Fig. 2 (b). We find two conduction bands Λ_2 and Λ_3 possess negative and positive eigenvalues, respectively, and the conduction band Λ_1 has positive eigenvalue. Thus, at σ_v invariant plane MKHL, the band crossings of Λ_2 and Λ_1 are mirror symmetry protected and form a nodal line structure (NL3). On the contrary, the band crossings between band Λ_3 and Λ_1 are avoidable because of the same eigenvalues of σ_v. Considering the C_{3z} rotation of HKH′ axis, three equivalent NL3 emerge and connect to each other exactly at the TDPs. As schematically shown in Fig. 2 (e), the NL3 structure at extended MKHL plane is not eudipleural with respect to HKH′ axis and noted as an off-centered nodal ring because of polar C_{3z} symmetry. In addition, the NL1 and NL2 at $k_z = 0$ plane interconnect with three vertical NL3 from inside and outside, respectively, thus forming a cage-like node structure encircling K point. This unique nodal line interconnection makes this ferromagnetic triplet fermion distinguished from other known TDP semimetal states.[48]

When the SOC effect is included with (001) magnetization, the little group along H-K-H′ is lowered to C_3 that can not guarantee a two-dimensional representation any more. As a consequence, the doubly degenerate conduction band Γ_3 in Fig. 2 (a) splits into two singlet states (Γ_{31} and Γ_{32}) in Fig. 2 (c). Accordingly, a pair of TDPs are splitting into two pairs of WPs along H-K-H′ path. By calculating the charities of the WPs, we identify that the WPs between Γ_{32} and Γ_2 are double Weyl points (DWPs, C = ± 2) while the WPs between Γ_{31} and Γ_2 are single Weyl points (SWPs, C = ± 1). Remarkably, the strong SOC effect in ferromagnetic Eu_5Bi_3 transforms a triplet point into two WPs with different charities. We have identified the distinctive charities stem from distinctive eigenvalues of C_3 operation for Γ_{31} and Γ_{32}.[62] On the other hand, the SOC breaks σ_h symmetry but reserves σ_v symmetry.

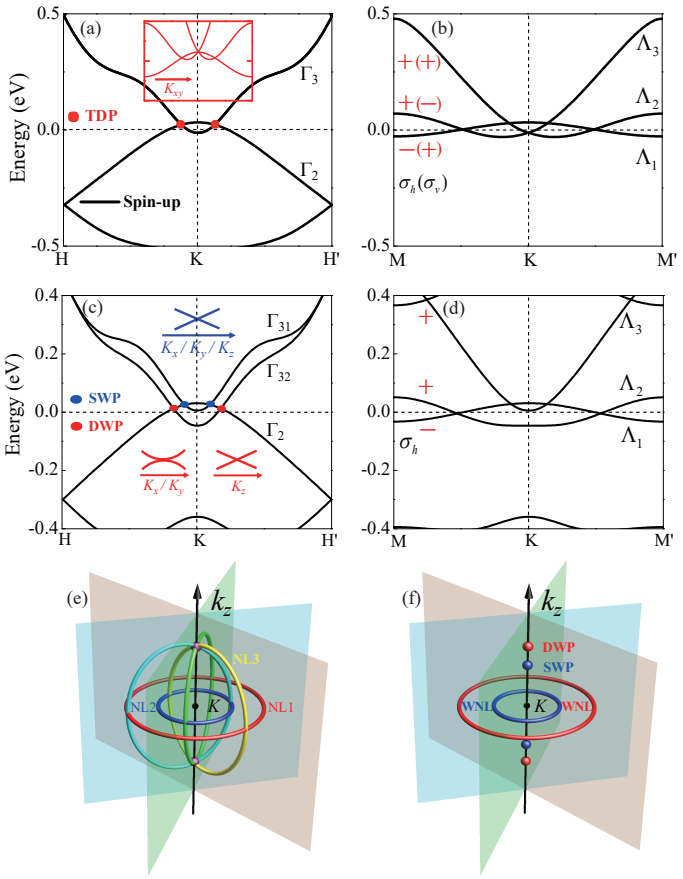

Figure 2: Band structures of Eu_5Bi_3 focusing on K point. Spin-up/SOC band structures of Eu_5Bi_3 along high-symmetry (a)/(c) H-K-H′ and (b)/(d) M-K-M′ paths. K_{xy} direction is parallel to $k_x + k_y$ direction. Mirror eigenvalues of σ_h and σ_v are labeled in figure (b) and (d). (e) and (f) show the 3D view of the band crossing points around K point with and without SOC, respectively. The Fermi level is shifted to zero in (a), (b), (c) and (d).

Therefore, the NL3 is broken but NL1 and NL2 are reserved. As schematically demonstrated in Fig. 2 (f), the Eu_5Bi_3 system simultaneously host 0D WPs and 1D WNLs coupled around K point, thus forming a new type of WNPL Fermion around the Fermi level. This composite fermion is quite different from other's proposals of a simple coexistence of WPs and WNL without physical relevance.[63,64] The composite WNPL fermion in Eu_5Bi_3 is derived from band inversion and protected by C_{6v} point group. Our low-energy effective $\boldsymbol{k} \cdot \boldsymbol{p}$ model will further reveal the intrinsic coupling nature of the WNPL fermion.

In fact, the ferromagnetic Eu_5Bi_3 host two sets of WNPL structures centred at K point. As schematically plotting in Fig. 2 (f), one is composed of a pair of DWPs and a WNL

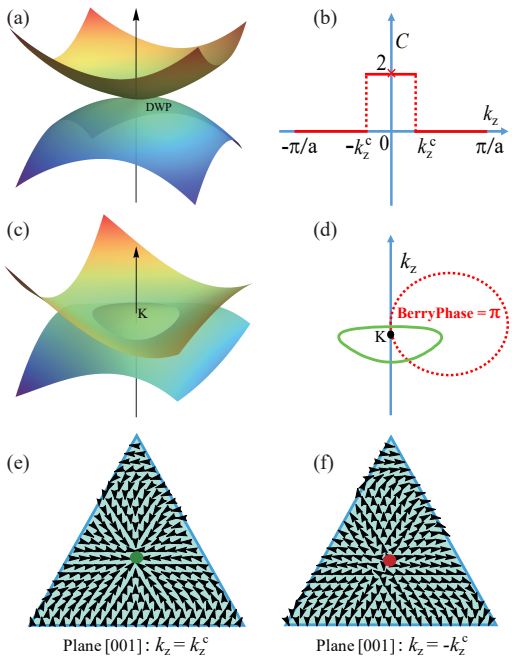

Figure 3: 3D view of the band dispersions of (a) DWP and (c) WNL. (b) Schematic of the Chern number as a function of k_z along H-K-H′ direction. (d) Quantized Berry phase of a arbitrary loop intersect a target WNL with magnetization parallel to [001] direction. (e) and (f) show the distribution of the Berry curvature of DWP with negative and positive chirality at $k_z = k_z^c$ and $k_z = -k_z^c$ plane, respectively.

structure (red color), and the other is consisted of a pair of SWPs and a WNL structure (blue color). Here, taking the first WNPL structure (closer to Fermi level) for example, the corresponding two-band effective $\boldsymbol{k}\cdot\boldsymbol{p}$ model can be written as[62]

$$\begin{aligned}\mathcal{H}(\boldsymbol{k}) &= \left(A\boldsymbol{k}_{//}^2 + ak_z^2 + m_0\right)\sigma_0 + Bk_z\left(k_-^2\sigma_+ + k_+^2\sigma_-\right) \\ &+ \left[D\boldsymbol{k}_{//}^2 + dk_z^2 + m + Ck_x\left(k_x^2 - 3k_y^2\right)\right]\sigma_z, \end{aligned} \quad (1)$$

where σ_0 is the identity matrix and $\sigma_\pm = \sigma_x \pm i\sigma_y$ with $\sigma_{x,y,z}$ to be the Pauli matrices. The $\boldsymbol{k}_{//}$ is the in-plane momentum, the A, B, C, D, a, d, m, m_0 are fitting parameters from first-principles calculations. By solving this Hamiltonian, we can obtain a pair of DWPs located at (0, 0, $k_z^c = \pm\sqrt{-m/d}$) and a WNL in $k_z = 0$ plane when the conditions $d{\cdot}m < 0$ and $D{\cdot}m < 0$ are satisfied. The 3D energy dispersions of DWP at $k_z = k_z^c$ and WNL in $k_z = 0$ plane are plotted in Fig. 3 (a) and (c). The DWP at $k_z = k_z^c$ possesses a quadratic in-plane

dispersion with chirality of +2. For any planes with fixed k_z (except $k_z = 0, \pm k_z^c$), the system becomes an insulator and a k_z-dependent chern number can be well defined as shown in Fig. 3 (b), where the +2 chern number appears in the region of $-k_z^c < k_z < k_z^c$ that confirms it is a DWP. The Berry curvature distributions of DWPs are demonstrated in Figs. 3 (e)-(f), in which the DWP work as a source or sink in the field of Berry curvature with triangular symmetry. In Fig. 3 (c), we notice the conduction and valence bands intersect around K point and produce a trigonal WNL structure at $k_z = 0$ plane. This interesting trigonal warping effect of the WNL structure is induced by the C_{3z} symmetry which is considered in $Ck_x\left(k_x^2 - 3k_y^2\right)$. As shown in Fig. 3 (b), the integral of Berry phase along an arbitrary closed path that interlocks the WNL indeed gives a π Berry phase.

Taking a close look at the Hamiltonian, the first term breaks the electron-hole symmetry and brings the energy difference of band crossings, but this term has no concern with the topological nature. The second term provides couplings for WNL and DWPs when momentum $\boldsymbol{k}$ is neither at $k_z = 0$ plane nor at k_z axis. The last term plays a vital role for the emergence of the nontrivial topological phase in Eu_5Bi_3. When $D{\cdot}m < 0$ and $d{\cdot}m < 0$, the band inversion happens, a DWPs and WNL fermion are produced concurrently to form a WNPL Fermion.

Based on the effective $\boldsymbol{k}\cdot\boldsymbol{p}$ model, we further explore the novel surface states and Fermi arcs of the WNPL fermion. As shown in Figs. 4 (b)-(d), we choose three representative projection planes (001), (100) and Ω. For the (001) surface as shown in Fig. 4 (b), a WNL can be projected with maximal area (region S_{001}, red dashed line), and two DWPs are projected into a same point $\overline{\mathrm{K}}$ at the center of region S_{001}. The "drumhead" surface state from the WNL structure emerges inside region S_{001} as shown in Figs. 4 (i)-(j). Remarkably, we find that along $\overline{\mathrm{M}}$-$\overline{\mathrm{K}}$-$\overline{\mathrm{M}}'$ path, the "drumhead" surface state must cross $\overline{\mathrm{K}}$ point regardless of the surface circumstance. In other words, this "drumhead" surface state of the WNL is naturally pinned by the DWPs.

For (100) projection plane as shown in Fig. 4 (c), the WNL is projected into a line

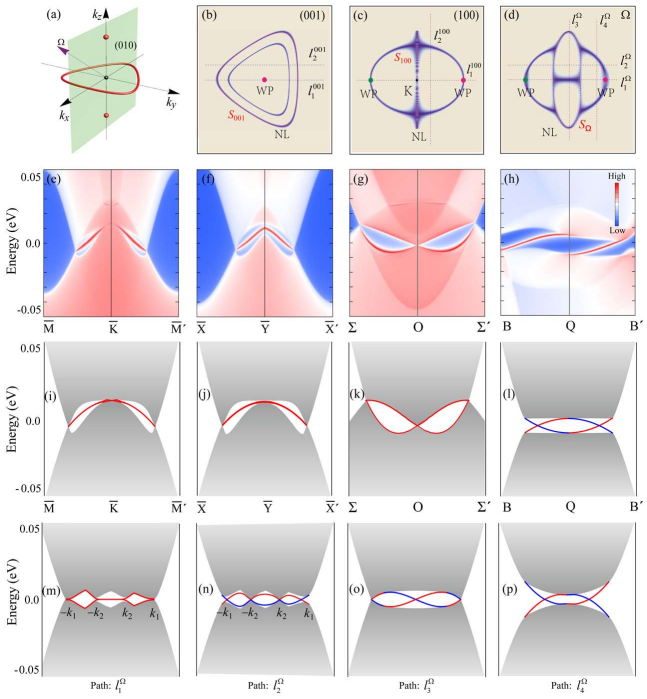

Figure 4: Surface states and Fermi arcs of WNPLSM. (a) Schematic illustrations of the WNPLSM in the 3D Brillouin zone. The normal direction of the Ω , i.e., the purple arrow is lying in the k_x-k_z plane that is highlighted in lightgreen. (b), (c) and (d) show the calculated Fermi arcs of Eu_5Bi_3 for (001), (100) and Ω planes, respectively. Paths l_1^{001}, l_2^{001}, l_1^{100}, l_2^{100} are equal to paths $\overline{\text{M}}$-$\overline{\text{K}}$-$\overline{\text{M}}'$, $\overline{\text{M}}$-$\overline{\text{K}}$-$\overline{\text{M}}'$, Σ-O-Σ′, B-Q-B′. (e)-(h) and (i)-(l) Surface band structures projected onto (001) and (100) planes calculated by wannier function and $\boldsymbol{k}\cdot\boldsymbol{p}$ Hamiltonian, respectively. (m)-(p) Surface band structures projected onto Ω plane calculated by $\boldsymbol{k}\cdot\boldsymbol{p}$ Hamiltonian.

segment (line S_{100}, red dashed line) and two DWPs are projected into both sides of line segment S_{100}. As shown in Fig. 4 (l), along B-O-B′ path, we can clearly see two branches of surface states with same chirality connect the conduction and valence bands, in good agreement with our calculated charity (±2) of DWPs. As shown in in Fig. 4 (k), along Σ-O-Σ′ path that connects two DWPs and crosses the WNL, we notice the surface states have to cross each other at WNL projection position, thus showing that the chiral surface states of DWPs are nontrivially pinned by the WNL structure. The Fermi surface of (100) surface state is displayed in Fig. 4 (c). Two Fermi arcs stem from one DWP and cross both ends of the WNL projection region, and then gather together at the other DWP. This unique connection of surface Fermi arcs further demonstrates the coupling of DWPs and WNL in

the WNPL fermion. These surface band structures of (001) and (100) projection planes are detailedly checked by our DFT calculations as shown in Figs. 4 (e)-(h). Same morphologies of the surface states of WNPL fermion are revealed by DFT calculations, which matches well with that from $\boldsymbol{k} \cdot \boldsymbol{p}$ model.

For a general projection plane Ω as shown in Fig. 4 (d), the WNL structure is projected into a small area (region S_Ω, red dashed line) and two DWPs are projected into both sides of region S_Ω. To get a global view of the coupled surface state, we chose four k-paths ($l^\Omega_{1,2,3,4}$) and corresponding surface states are listed in Figs. 4 (m)-(p). First for l^Ω_1 path in Fig. 4 (m), two surface states from DWP emerge at $-k_1$ point and connect to the WNL at $-k_2$ point, similar to that in Fig. 4 (k). Inside the WNL projection region $[-k_2, k_2]$, the surface state shows nearly flat dispersion. When l^Ω_1 path is parallelly moved to l^Ω_2 as shown in Fig. 4 (n), the WP's surface states still exist between k_1 and k_2, but the flat WNL's surface state becomes bended in region $[-k_2, k_2]$. This bending effect can be clearly observed along a vertical path l^Ω_3 as shown in Fig. 4 (o), where we can see the surface state on the top surface (red line) and on the bottom surface (blue line) possess opposite Fermi velocities. This means the surface state inside the WNL's projection region S_Ω also carries charity, denoted as chiral WNL surface states in WNPL structure. When l^Ω_3 path is parallelly shifted to l^Ω_4 outside S_Ω, two chiral surface states from the DWPs connect the conduction and valence bands similar with that in Fig. 4 (l). By plotting the Fermi surface of the surface state on Ω plane in Fig. 4 (d), we reveal two Fermi arcs stemming from two DWPs connect to the boundary of S_Ω. Inside S_Ω region, a new Fermi arc emerges which derived from the chiral surface state in WNPL structure. Those unique chiral WNL surface states and fascinating links of surface Fermi arcs are significant characteristics that can discriminate the WNPL fermion from individual WP or WNL fermions.

The Weyl fermion in solid was initially proposed in a magnetic $YIrO_3$[39] but firstly experimentally observed in nonmagnetic TaAs families.[23] In contrast with Weyl fermions in nonmagnetic materials, the magnetic Weyl fermions have the following advantages: (1) the

least number of WPs, (2) the larger separation in reciprocal space for two WPs with opposite charities, (3) the giant anomalous Hall effect derived from the diverging Berry curvature of WPs.[59,60,65] The Weyl fermion proposed in ferromagnetic Eu_5Bi_3 perfectly meets these superiorities. Specifically, the system hosts a pair of WPs in momentum space with a big interval of 0.15 $Å^{-1}$ and a large anomalous Hall conductivity of -260 $(\hbar/e)(\Omega\text{cm})^{-1}$ parallel to [001] direction is predicted.

In conclusion, we propose a new type TSM state, WNPL fermion, which is characterized by the intrinsic coexistence of WPs and WNL. We discover a SOC driven topological phase transition from magnetic TDP semimetal to WNPL semimetal in hexagonal Eu_5Bi_3. The exotic surface state of WNPL fermion including pinned chiral surface state and unique linked Fermi arcs are demonstrated by both DFT calculations and effective $\boldsymbol{k}\cdot\boldsymbol{p}$ model. Our work sheds light on discovering new topological semimetal states from diverse band-crossing dimensions, and point to an ideal material candidate Eu_5Bi_3 for future experimental realization. We believe this composite WNPL fermion can be further generalized to Weyl nodal point-surface and line-surface fermions.

Acknowledgement

This work is supported by the National Key R&D Program of China (Grant No. 2016YFA0300600), the National Natural Science Foundation of China (Grants No. 11734003, No. 11574029), the Strategic Priority Research Program of Chinese Academy of Sciences (Grant No. XDB30000000), the Fundamental Research Funds for the Central Universities (Grant No.2017CX10007). B.T.F. also thanks Sichuan Normal University for financial support (No. 341829001). H.B.W. and D.S.M. also thank the supports from Graduate Technological Innovation Project of Beijing Institute of Technology (Grant No. 2018CX10028).

H.B.W. and D.S.M. contributed equally to this work.

Supporting Information

Supporting Information Available: The computational methods and details for the constructions of the $\boldsymbol{k} \cdot \boldsymbol{p}$ effective Hamiltonian.

References

1. Armitage, N.; Mele, E.; Vishwanath, A. Weyl and Dirac semimetals in three-dimensional solids. *Rev. Mod. Phys.* **2018**, *90*, 015001.

2. Young, S. M.; Zaheer, S.; Teo, J. C.; Kane, C. L.; Mele, E. J.; Rappe, A. M. Dirac semimetal in three dimensions. *Phys. Rev. Lett.* **2012**, *108*, 140405.

3. Wang, Z.; Sun, Y.; Chen, X.-Q.; Franchini, C.; Xu, G.; Weng, H.; Dai, X.; Fang, Z. Dirac semimetal and topological phase transitions in A_3Bi (A= Na, K, Rb). *Phys. Rev. B* **2012**, *85*, 195320.

4. Xu, S.-Y.; Belopolski, I.; Alidoust, N.; Neupane, M.; Bian, G.; Zhang, C.; Sankar, R.; Chang, G.; Yuan, Z.; Lee, C.-C. et al. Discovery of a Weyl fermion semimetal and topological Fermi arcs. *Science* **2015**, *349*, 613–617.

5. Chen, Y.; Xie, Y.; Yang, S. A.; Pan, H.; Zhang, F.; Cohen, M. L.; Zhang, S. Nanostructured Carbon Allotropes with Weyl-like Loops and Points. *Nano Lett.* **2015**, *15*, 6974–6978.

6. Weng, H.; Dai, X.; Fang, Z. Topological semimetals predicted from first-principles calculations. *J. Phys.: Condens. Matter.* **2016**, *28*, 303001.

7. Chiu, C.-K.; Teo, J. C.; Schnyder, A. P.; Ryu, S. Classification of topological quantum matter with symmetries. *Rev. Mod. Phys.* **2016**, *88*, 035005.

8. Huang, H.; Jin, K.-H.; Zhang, S.; Liu, F. Topological Electride Y_2C. *Nano Lett.* **2018**, *18*, 1972–1977.

9. Hirayama, M.; Okugawa, R.; Murakami, S. Topological semimetals studied by ab initio calculations. *J. Phys. Soc. Jpn.* **2018**, *87*, 041002.

10. Jiang, Y.; Dun, Z.; Moon, S.; Zhou, H.; Koshino, M.; Smirnov, D.; Jiang, Z. Landau Quantization in Coupled Weyl Points: A Case Study of Semimetal NbP. *Nano Lett.* **2018**, *18*, 7726–7731.

11. Zyuzin, A.; Burkov, A. Topological response in Weyl semimetals and the chiral anomaly. *Phys. Rev. B* **2012**, *86*, 115133.

12. Son, D.; Spivak, B. Chiral anomaly and classical negative magnetoresistance of Weyl metals. *Phys. Rev. B* **2013**, *88*, 104412.

13. Gorbar, E.; Miransky, V.; Shovkovy, I. Chiral anomaly, dimensional reduction, and magnetoresistivity of Weyl and Dirac semimetals. *Phys. Rev. B* **2014**, *89*, 085126.

14. Huang, X.; Zhao, L.; Long, Y.; Wang, P.; Chen, D.; Yang, Z.; Liang, H.; Xue, M.; Weng, H.; Fang, Z. et al. Observation of the chiral-anomaly-induced negative magnetoresistance in 3D Weyl semimetal TaAs. *Phys. Rev. X* **2015**, *5*, 031023.

15. Heikkilä, T. T.; Kopnin, N. B.; Volovik, G. E. Flat bands in topological media. *JETP Lett.* **2011**, *94*, 233.

16. Qi, Y.; Naumov, P. G.; Ali, M. N.; Rajamathi, C. R.; Schnelle, W.; Barkalov, O.; Hanfland, M.; Wu, S.-C.; Shekhar, C.; Sun, Y. et al. Superconductivity in Weyl semimetal candidate $MoTe_2$. *Nat. Commun.* **2016**, *7*, 11038.

17. Chan, Y.-H.; Chiu, C.-K.; Chou, M.; Schnyder, A. P. Ca_3P_2 and other topological semimetals with line nodes and drumhead surface states. *Phys. Rev. B* **2016**, *93*, 205132.

18. Wang, Y.; Nandkishore, R. M. Topological surface superconductivity in doped Weyl loop materials. *Phys. Rev. B* **2017**, *95*, 060506.

19. Brüne, C.; Liu, C.; Novik, E.; Hankiewicz, E.; Buhmann, H.; Chen, Y.; Qi, X.; Shen, Z.; Zhang, S.; Molenkamp, L. Quantum Hall effect from the topological surface states of strained bulk HgTe. *Phys. Rev. Lett.* **2011**, *106*, 126803.

20. Wang, C.; Sun, H.-P.; Lu, H.-Z.; Xie, X. 3D quantum Hall effect of Fermi arcs in topological semimetals. *Phys. Rev. Lett.* **2017**, *119*, 136806.

21. Zhang, C.; Zhang, Y.; Yuan, X.; Lu, S.; Zhang, J.; Narayan, A.; Liu, Y.; Zhang, H.; Ni, Z.; Liu, R. et al. Quantum Hall effect based on Weyl orbits in Cd_3As_2. *Nature* **2018**, 1.

22. Burkov, A.; Balents, L. Weyl semimetal in a topological insulator multilayer. *Phys. Rev. Lett.* **2011**, *107*, 127205.

23. Lv, B.; Weng, H.; Fu, B.; Wang, X.; Miao, H.; Ma, J.; Richard, P.; Huang, X.; Zhao, L.; Chen, G. et al. Experimental discovery of Weyl semimetal TaAs. *Phys. Rev. X* **2015**, *5*, 031013.

24. Soluyanov, A. A.; Gresch, D.; Wang, Z.; Wu, Q.; Troyer, M.; Dai, X.; Bernevig, B. A. Type-II weyl semimetals. *Nature* **2015**, *527*, 495.

25. Burkov, A.; Hook, M.; Balents, L. Topological nodal semimetals. *Phys. Rev. B* **2011**, *84*, 235126.

26. Mullen, K.; Uchoa, B.; Glatzhofer, D. T. Line of Dirac nodes in hyperhoneycomb lattices. *Phys. Rev. Lett.* **2015**, *115*, 026403.

27. Fang, C.; Weng, H.; Dai, X.; Fang, Z. Topological nodal line semimetals. *Chin. Phys. B* **2016**, *25*, 117106.

28. Hu, J.; Tang, Z.; Liu, J.; Liu, X.; Zhu, Y.; Graf, D.; Myhro, K.; Tran, S.; Lau, C. N.; Wei, J. et al. Evidence of topological nodal-line fermions in ZrSiSe and ZrSiTe. *Phys. Rev. Lett.* **2016**, *117*, 016602.

29. Li, S.; Yu, Z.-M.; Liu, Y.; Guan, S.; Wang, S.-S.; Zhang, X.; Yao, Y.; Yang, S. A. Type-II nodal loops: Theory and material realization. *Phys. Rev. B* **2017**, *96*, 081106.

30. Fang, C.; Chen, Y.; Kee, H.-Y.; Fu, L. Topological nodal line semimetals with and without spin-orbital coupling. *Phys. Rev. B* **2015**, *92*, 081201.

31. Zhong, C.; Chen, Y.; Xie, Y.; Yang, S. A.; Cohen, M. L.; Zhang, S. Towards three-dimensional Weyl-surface semimetals in graphene networks. *Nanoscale* **2016**, *8*, 7232–7239.

32. Liang, Q.-F.; Zhou, J.; Yu, R.; Wang, Z.; Weng, H. Node-surface and node-line fermions from nonsymmorphic lattice symmetries. *Phys. Rev. B* **2016**, *93*, 085427.

33. Bzdušek, T.; Sigrist, M. Robust doubly charged nodal lines and nodal surfaces in centrosymmetric systems. *Phys. Rev. B* **2017**, *96*, 155105.

34. Weng, H.; Fang, C.; Fang, Z.; Bernevig, B. A.; Dai, X. Weyl semimetal phase in noncentrosymmetric transition-metal monophosphides. *Phys. Rev. X* **2015**, *5*, 011029.

35. Yan, B.; Felser, C. Topological materials: Weyl semimetals. *Annu. Rev. Condens. Matter Phys.* **2017**, *8*, 337–354.

36. Burkov, A. Weyl metals. *Annu. Rev. Condens. Matter Phys.* **2018**, *9*, 359–378.

37. Wang, R.; Zhao, J.; Jin, Y.; Du, Y.; Zhao, Y.; Xu, H.; Tong, S. Nodal line fermions in magnetic oxides. *Phys. Rev. B* **2018**, *97*, 241111.

38. Feng, B.; Zhang, R.-W.; Feng, Y.; Fu, B.; Wu, S.; Miyamoto, K.; He, S.; Chen, L.; Wu, K.; Shimada, K. et al. Discovery of Weyl nodal lines in a single-layer ferromagnet. *arXiv:1901.01429* **2019**,

39. Wan, X.; Turner, A. M.; Vishwanath, A.; Savrasov, S. Y. Topological semimetal and Fermi-arc surface states in the electronic structure of pyrochlore iridates. *Phys. Rev. B* **2011**, *83*, 205101.

40. Hasan, M. Z.; Xu, S.-Y.; Belopolski, I.; Huang, S.-M. Discovery of Weyl fermion semimetals and topological Fermi arc states. *Annu. Rev. Condens. Matter Phys.* **2017**, *8*, 289–309.

41. Belopolski, I.; Xu, S.-Y.; Ishida, Y.; Pan, X.; Yu, P.; Sanchez, D. S.; Zheng, H.; Neupane, M.; Alidoust, N.; Chang, G. et al. Fermi arc electronic structure and Chern numbers in the type-II Weyl semimetal candidate $Mo_xW_{1-x}Te_2$. *Phys. Rev. B* **2016**, *94*, 085127.

42. Deng, K.; Wan, G.; Deng, P.; Zhang, K.; Ding, S.; Wang, E.; Yan, M.; Huang, H.; Zhang, H.; Xu, Z. et al. Experimental observation of topological Fermi arcs in type-II Weyl semimetal $MoTe_2$. *Nat. Phys.* **2016**, *12*, 1105.

43. Fang, C.; Gilbert, M. J.; Dai, X.; Bernevig, B. A. Multi-Weyl topological semimetals stabilized by point group symmetry. *Phys. Rev. Lett.* **2012**, *108*, 266802.

44. Jian, S.-K.; Yao, H. Correlated double-Weyl semimetals with Coulomb interactions: Possible applications to $HgCr_2Se_4$ and $SrSi_2$. *Phys. Rev. B* **2015**, *92*, 045121.

45. Huang, S.-M.; Xu, S.-Y.; Belopolski, I.; Lee, C.-C.; Chang, G.; Chang, T.-R.; Wang, B.; Alidoust, N.; Bian, G.; Neupane, M. et al. New type of Weyl semimetal with quadratic double Weyl fermions. *Proc. Natl. Acad. Sci. USA* **2016**, *113*, 1180–1185.

46. Tsirkin, S. S.; Souza, I.; Vanderbilt, D. Composite Weyl nodes stabilized by screw symmetry with and without time reversal. *Phys. Rev. B 96*, 045102.

47. Zaheer, S.; Young, S. M.; Cellucci, D.; Teo, J. C.; Kane, C. L.; Mele, E. J.; Rappe, A. M.

Spin texture on the Fermi surface of tensile-strained HgTe. *Phys. Rev. B* **2013**, *87*, 045202.

48. Weng, H.; Fang, C.; Fang, Z.; Dai, X. Topological semimetals with triply degenerate nodal points in θ-phase tantalum nitride. *Phys. Rev. B* **2016**, *93*, 241202.

49. Winkler, G. W.; Wu, Q.; Troyer, M.; Krogstrup, P.; Soluyanov, A. A. Topological phases in $InAs_{1-x}Sb_x$: from novel topological semimetal to Majorana wire. *Phys. Rev. Lett.* **2016**, *117*, 076403.

50. Zhu, Z.; Winkler, G. W.; Wu, Q.; Li, J.; Soluyanov, A. A. Triple point topological metals. *Phys. Rev. X* **2016**, *6*, 031003.

51. Yang, H.; Yu, J.; Parkin, S. S.; Felser, C.; Liu, C.-X.; Yan, B. Prediction of triple point fermions in simple half-Heusler topological insulators. *Phys. Rev. Lett.* **2017**, *119*, 136401.

52. Gao, W.; Zhu, X.; Zheng, F.; Wu, M.; Zhang, J.; Xi, C.; Zhang, P.; Zhang, Y.; Hao, N.; Ning, W. et al. A possible candidate for triply degenerate point fermions in trigonal layered $PtBi_2$. *Nat. Commun.* **2018**, *9*.

53. Zhang, T.-T.; Yu, Z.-M.; Guo, W.; Shi, D.; Zhang, G.; Yao, Y. From Type-II Triply Degenerate Nodal Points and Three-Band Nodal Rings to Type-II Dirac Points in Centrosymmetric Zirconium Oxide. *J. Phys. Chem. Lett.* **2017**, *8*, 5792–5797.

54. Neupane, M.; Belopolski, I.; Hosen, M. M.; Sanchez, D. S.; Sankar, R.; Szlawska, M.; Xu, S.-Y.; Dimitri, K.; Dhakal, N.; Maldonado, P. et al. Observation of topological nodal fermion semimetal phase in ZrSiS. *Phys. Rev. B* **2016**, *93*, 201104.

55. Bian, G.; Chang, T.-R.; Sankar, R.; Xu, S.-Y.; Zheng, H.; Neupert, T.; Chiu, C.-K.; Huang, S.-M.; Chang, G.; Belopolski, I. et al. Topological nodal-line fermions in spin-orbit metal $PbTaSe_2$. *Nat. Commun.* **2016**, *7*, 10556.

56. Wang, X.; Pan, X.; Gao, M.; Yu, J.; Jiang, J.; Zhang, J.; Zuo, H.; Zhang, M.; Wei, Z.; Niu, W. et al. Evidence of both surface and bulk Dirac bands and anisotropic nonsaturating magnetoresistance in ZrSiS. *Adv. Electron. Mater.* **2016**, *2*, 1600228.

57. Gao, Z.; Hua, M.; Zhang, H.; Zhang, X. Classification of stable Dirac and Weyl semimetals with reflection and rotational symmetry. *Phys. Rev. B* **2016**, *93*, 205109.

58. Yang, S.-Y.; Yang, H.; Derunova, E.; Parkin, S. S. P.; Yan, B.; Ali, M. N. Symmetry Demanded Topological Nodal-line Materials. *Adv. Phys.: X* **2018**, *3*, 1414631.

59. Kim, K.; Seo, J.; Lee, E.; Ko, K.-T.; Kim, B.; Jang, B. G.; Ok, J. M.; Lee, J.; Jo, Y. J.; Kang, W. et al. Large anomalous Hall current induced by topological nodal lines in a ferromagnetic van der Waals semimetal. *Nat. Mater.* **2018**, *17*, 794.

60. Wang, Q.; Xu, Y.; Lou, R.; Liu, Z.; Li, M.; Huang, Y.; Shen, D.; Weng, H.; Wang, S.; Lei, H. Large intrinsic anomalous Hall effect in half-metallic ferromagnet $Co_3Sn_2S_2$ with magnetic Weyl fermions. *Nat. Commun.* **2018**, *9*, 3681.

61. Leon-Escamilla, E. A.; Corbett, J. D. Hydrogen in polar intermetallics. Binary pnictides of divalent metals with Mn_5Si_3-type structures and their isotypic ternary hydride solutions. *Chemistry of materials* **2006**, *18*, 4782–4792.

62. See Supplemental Material for the computational methods and details for the constructions of the $\boldsymbol{k} \cdot \boldsymbol{p}$ effective Hamiltonian.

63. Rauch, T.; Minh, H. N.; Henk, J.; Mertig, I. Model for ferromagnetic Weyl and nodal line semimetals: Topological invariants, surface states, anomalous and spin Hall effect. *Phys. Rev. B* **2017**, *96*, 235103.

64. Sun, J. P.; Zhang, D.; Chang, K. Coexistence of topological nodal lines, Weyl points, and triply degenerate points in TaS. *Phys. Rev. B* **2017**, *96*, 045121.

65. Yang, K.-Y.; Lu, Y.-M.; Ran, Y. Quantum Hall effects in a Weyl semimetal: Possible application in pyrochlore iridates. *Phys. Rev. B* **2011**, *84*, 075129.